Research Article | Vol. 12, No. 6 / 1 June 2021 / Biomedical Optics Express 3265
Biomedical Optics EXPRESS

Recipes for diffuse correlation spectroscopy instrument design using commonly utilized hardware based on targets for signal-to-noise ratio and precision

LORENZO CORTESE,[1,8,*] GIUSEPPE LO PRESTI,[1,8] MARCO PAGLIAZZI,[1] DAVIDE CONTINI,[2] ALBERTO DALLA MORA,[2] HAMID DEHGHANI,[3] FABIO FERRI,[4] JONAS B. FISCHER,[1,5] MARTINA GIOVANNELLA,[1] FABRIZIO MARTELLI,[6] UDO M. WEIGEL,[5] STANISLAW WOJTKIEWICZ,[3] MARTA ZANOLETTI,[1,2] AND TURGUT DURDURAN[1,7]

[1]*ICFO-Institut de Ciències Fotòniques, The Barcelona Institute of Science and Technology, 08860 Castelldefels (Barcelona), Spain*
[2]*Politecnico di Milano, Dipartimento di Fisica, 20133 Milano, Italy*
[3]*University of Birmingham, School of Computer Science, Edgbaston, Birmingham, B15 2TT, UK*
[4]*Università degli Studi dell'Insubria, Dipartimento di Scienza e Alta Tecnologia and To. Sca. Lab., 22100 Como, Italy*
[5]*HemoPhotonics S.L., 08860 Castelldefels (Barcelona), Spain*
[6]*Università degli Studi di Firenze, Dipartimento di Fisica, 50100 Firenze, Italy*
[7]*Institució Catalana de Recerca i Estudis Avançats (ICREA), 08015 Barcelona, Spain*
[8]*These authors equally contributed to this work. Authors are listed in alphabetical order except for the first three and the last*
[*]*lorenzo.cortese@icfo.eu*

Abstract: Over the recent years, a typical implementation of diffuse correlation spectroscopy (DCS) instrumentation has been adapted widely. However, there are no detailed and accepted recipes for designing such instrumentation to meet pre-defined signal-to-noise ratio (SNR) and precision targets. These require specific attention due to the subtleties of the DCS signals. Here, DCS experiments have been performed using liquid tissue simulating phantoms to study the effect of the detected photon count-rate, the number of parallel detection channels and the measurement duration on the precision and SNR to suggest scaling relations to be utilized for device design.

1. Introduction

Diffuse correlation spectroscopy (DCS) is an emerging diffuse optical modality based on the propagation of coherent near-infrared light deep into tissues in order to non-invasively monitor and/or image microvascular blood flow [1–3]. A typical DCS device records the intensity auto-correlation function of the speckle fluctuations and uses a correlation diffusion model of photon propagation in tissues that describes its statistics relating it to the dynamics of the moving scatterers. This signal is dominated by the motion of red blood cells in tissues, which, in turn, allows the researchers to estimate the microvascular blood flow in the probed tissue volume.

Nowadays, DCS has found a wide range of clinical applications [3–6], as for example in evaluating the response to functional stimuli in the brain [7–9], adult and infant brain monitoring for clinical research [10–13], for cancer diagnosis and cancer therapy monitoring [14–17], for studying muscle function [18,19], and for intra-operative monitoring [20–22]. All these applications have different requirements in speed, signal-to-noise ratio (SNR), precision (a measure of random errors or statistical variability leading to reduced repeatability and reproducibility)

#423071 https://doi.org/10.1364/BOE.423071
Journal © 2021 Received 22 Feb 2021; revised 18 Apr 2021; accepted 4 May 2021; published 11 May 2021

Biomedical Optics EXPRESS

and trueness [23] (also commonly named "accuracy" [24], a measure of systematic errors in obtaining the true value).

In this work, we will focus on a canonical DCS system/device that has previously been detailed in terms of the requirements for its major components - source, detector, fibers and correlator [5]. We have opted to limit the scope of this work to this approach that we called a "canonical DCS device and components" in order to provide not only a guidance for future designs but also for understanding the previous literature. Less common, but promising, approaches such as the use of different data types (e.g., speckle contrast) [25–28], the use of interferometry [29–31], the change of the wavelength [32,33] and time-resolved methods as well as the use of quasi-null source-detector separation [33–36] are not detailed here but they share many of the salient features of this work [37].

In a canonical DCS system, the precision in determining the blood flow is limited by several factors, such as the inherent sensitivity to probe movements, the influence of the probe pressure over the soft tissues, the low intensity of the detected signal, the incorrect determination of the optical properties of the tissue and possible cross-talk with other techniques (e.g near-infrared spectroscopy (NIRS)) that are performed simultaneously [3,38–40]. DCS signals are intrinsically more complex than the typical NIRS signals and also of other experiments involving the detection of photons, since the signal-to-noise ratio and the resulting precision involves and inter-play of the speckle statistics as well as the photon statistics [38,41–43]. These were partially addressed or alluded to in different works that are cited.

The main limitation tends to be the detected light intensity which arises from the necessity to investigate the hemodynamics of deep tissues, e.g., greater than a centimeter deep, which is achieved by using source to detector fiber separations of several centimeters (2.5 cm is common in DCS [3,44]. In principle, high quality measurements can be obtained by increasing the photon count-rate (i.e., by increasing the injected light intensity) [42,43,45]. This situation is often impossible to be met in a real clinical scenario due to maximum permissible exposure limits for tissues which can be relaxed only under extreme conditions.

If the injected power is limited, then, when measuring tissues that are more absorbing than others, e.g., the thyroid [17], the SNR and the precision are inherently lower unless longer averaging times are allowed. However, longer averaging times pose other restrictions. When measuring static properties such as that for cancer screening, the physiological variations and noise, and, patient comfort pose limits on the order of several seconds. On the other hand, many measurements, such as those used for cerebral blood flow monitoring require higher temporal resolution, even at tens of hertz [38,46–48], which are prohibitive even when the tissue absorption is not as high as the thyroid. Furthermore, even lower injection laser power, and consequently a lower detected photon count-rate may be required when the exposed tissue is sensitive, for example the skin of the premature born infant [10,49], where the injected laser radiation can induce temperature changes and tissue damage [50].

A more realistic method to improve the quality of DCS acquisitions is by adding a number of detection channels [38] probing independent speckles in the very same region of the tissue. The need for sampling individual, independent speckles implied that most DCS experiments utilize single- or few-mode fibers with diameters at few tens of micrometers [5,51]. We stress here that the addition of different detectors are due to the need to sample independent speckles rather than light collection from a larger volume as is typically done for NIRS experiments. Unfortunately, DCS detectors that fit all the requirements, including the quantum efficiency at the near-infrared window are, at the moment, costly and bulky. Scaling the number of detectors to meet the SNR and precision needs is, therefore, a non-trivial undertaking. Along these lines, it is notable that recently the development of dedicated low-cost hardware with arrays of single-photon detectors were proposed for multi-speckle DCS measurements but with the compromise of speed and quantum efficiency per channel [52–54].

Biomedical Optics EXPRESS

This work focuses on typical DCS hardware [5] and aims to provide recipes and guidance for current developers, buyers and users. Here the effect of key experimental parameters such as the measurement duration and the number of detection channels, at different photon count-rates are related to the precision of a DCS experiment, and the experimental results obtained have been analyzed considering the existing DCS noise theoretical models [38,42]. This provides a potential recipe in finding device and experimental settings that optimize the precision of the retrieved blood flow, balancing costs (that is, the number of the detectors necessary) and the temporal resolution.

2. Materials and methods

2.1. Experimental setup

The DCS module of a multi-modal instrument (so-called "LUCA device" [55], see also [56]), was utilized for this study. The source module consists of a single longitudinal mode continuous wave laser with wavelength of 785 *nm* (custom made by HemoPhotonics S. L., Castelldefels, ES). This laser has been compared with other common lasers used in DCS systems showing analogous quality in terms of stability and coherence (data provided by the manufacturer). The detection part is composed by sixteen single photon avalanche photodiodes (four modules of SPCM-AQ4C, Excelitas, U.S.), and a custom built sixteen channel hardware multi-tau autocorrelator (HP-CM16, HemoPhotonics S. L., Castelldefels, ES). Similarly, this correlator has been compared to the typical correlators utilized in DCS systems in the literature. Hence, this system can be considered a "canonical DCS system" as defined by Durduran and Yodh [5].

Light is injected into the sample through a multimode fiber with a 400 μm core (FP400ERT, Thorlabs, U.S.A.). A fiber optic attenuator (VOAMMF, Thorlabs, U.S.A.) is placed on the source side in order to tune the intensity of the light injected. The diffuse light is collected through a fiber bundle of sixteen single mode fibers with care taken to avoid cross-talk between fibers (custom designed by Fiberoptic Systems, U.S.A., with 780HP fibers by Thorlabs, U.S.A.). The collected photons from each fiber are independently measured by independent detectors. Finally, the single speckle intensity autocorrelation function (g_2) related to each detection channel is calculated in real time by the sixteen channel autocorrelator.

The source fiber and detection bundle cables have straight terminations (2.5 *mm* diameter ferrules) that are fixed, on the same side of the probe, at a distance of 2.5 *cm* from each other, in reflectance geometry. The probe consists of a black plastic support that, during the measurements, is kept in a fixed and stable position over the liquid surface of the phantom by the use of a mechanical support.

The phantom experiments have been performed using a dilution of Lipofundind20% in purified water (Milli-Q, Millipore, USA) as scattering element. The concentration of Lipofundin20% in water has been chosen in order to have a reduced scattering coefficient, μ_s', of 5 cm^{-1} and the absorption coefficient due to water without additional absorbers by following the recipe described in ref. [57]. The liquid solution has been placed in a black phantom box (size 20 $cm \times 30$ $cm \times 20$ cm) with the top side open in order to allow the access of the probe to the liquid. The DCS measurement consisted of hundred subsequent acquisitions of one second averaging each at a fixed detected photon count-rate. A range of count-rates between 5 kHz to 150 kHz have been utilized by attenuating the intensity of the light injected by the attenuator.

2.2. Data analysis

2.2.1. DCS theory

The particle, i.e., scatterer, Brownian diffusion coefficient (D_B) is the measure the DCS utilizes from liquid phantoms to evaluate its performance in a way akin to that of the tissues. D_B was retrieved by fitting the solution of the correlation diffusion equation for the electric field

Biomedical Optics EXPRESS

autocorrelation function for a semi-infinite medium, in reflectance geometry, at a determined time t_0 and source detector separation ρ, i.e.:

$$G_1(\rho, t_0, \tau) = \langle \mathbf{E}(\rho, t_0)\mathbf{E}^*(\rho, t_0 + \tau)\rangle = \frac{v}{4\pi D}\left[\frac{exp^{-K(\tau)r_+}}{r_+} - \frac{exp^{-K(\tau)r_-}}{r_-}\right] \quad (1)$$

where $D = \frac{v}{3\mu_s'}$ is the photon diffusion coefficient, τ is the delay time, $K(\tau) = \sqrt{(\mu_a + \mu_s' k_0^2 \alpha D_B \tau)\frac{v}{D}}$ is the decay constant, k_0 is the wavenumber in the medium, α is the fraction of moving scatterers with respect to the total scatterers (in the case of liquid phantom we assume $\alpha = 1$), $r_+ = \sqrt{\rho^2 + (\frac{1}{\mu_s'})^2}$, $r_- = \sqrt{\rho^2 + (-2z_e - \frac{1}{\mu_s'})^2}$, z_e is the extrapolation length $z_e = \frac{2}{3}\frac{1+R_{eff}}{1-R_{eff}}$, and R_{eff} is the effective reflection coefficient that accounts for the refractive index mismatch between the two media. In the experiments we have measured the normalized intensity correlation function $g_2(\rho, t_0, \tau) = \langle I(\rho, t_0)I(\rho, t_0 + \tau)\rangle / \langle I(\mathbf{r}, t_0)\rangle^2$. The intensity autocorrelation function g_2 is linked to the normalized electric field autocorrelation function $g_1(\rho, t_0, \tau) = G_1(\rho, t_0, \tau)/G_1(\rho, t_0, \tau = 0)$ through the Siegert relation [3] $g_2(\rho, t_0, \tau) = 1 + \beta\,|g_1(\rho, t_0, \tau)|^2$, where β is a parameter mainly related to the collection optics of the experiment and to the number of speckles in the detection area. In the fitting procedure, performed by using the Matlab function "fminsearch", the reduced scattering coefficient, the absorption coefficient and β were fixed values, and the only fitting parameter was D_B. In addition, in order to consider diffusing photons, only the first part of the g_1 has been considered to retrieve D_B [58] and the fitting interval has been limited up to $\tau = \tau_c$, where τ_c is such that $g_1(\tau_c) = 0.6$. In order to compare the effect of different count rates, i.e., the number of detected photons, on the results without further bias, we have avoided additional post-processing steps such as filtering or de-noising of the data.

2.2.2. Evaluation of DCS precision

For the evaluation of the precision, the data acquired in every measurement at a fixed detected count-rate were evaluated by calculating the coefficient of variation $CV = \sigma_{D_B}/\overline{D}_B$ (where σ_{D_B} is the standard deviation of the measured D_B, and $\overline{D}_B$ the average value) related to the retrieved D_B by considering a varying number of detectors (from 1 to 16) and different measurement durations.

For each detected photon count-rate, DCS measurements consisted of one hundred subsequent g_2 acquisitions of one second averaging each.

To retrieve the dependence of DCS precision on the measurement duration, we have proceeded as described in the illustration of block (a) of Fig. 1. First, for every detection channel, we have analyzed the g_2 by averaging subsequently from the first to the hundredth (that is, from one to one-hundred seconds). Then, the averaged curves have been fitted to retrieve the D_B. In this way, for every one of the 16 channels, we have obtained 100 different D_B values, the first one resulting from one g_2 curve (i.e., a one second measurement), the second one resulting from the average of two g_2 curves (i.e., a two second measurement), up to the hundredth, resulting from the average of one-hundred g_2 curves. Finally, the one-hundred average $\overline{D}_B$ and the coefficients of variation CV related to different measurement durations have been obtained by averaging the D_B over the acquisition channels for fixed measurement duration, and calculating the standard deviation (σ_{D_B}).

The procedure followed to retrieve the dependence of the measurement precision on the number of detection channels is described in Fig. 1(b).

For every channel, we have selected ten subsequent (time) slots of fixed duration, $t_1^x, \ldots, t_{10}^x$ among the one hundred acquired g_2, containing an equal number x of g_2. Then, all the g_2 curves inside a single interval t_i^x have been averaged and then averaged again considering subsequently a different number of detection channels, ranging from 1 to 16. The resulting curves (one for each time slot t_i^x) have been fitted to retrieve the Brownian diffusion coefficient D_B.

Biomedical Optics EXPRESS

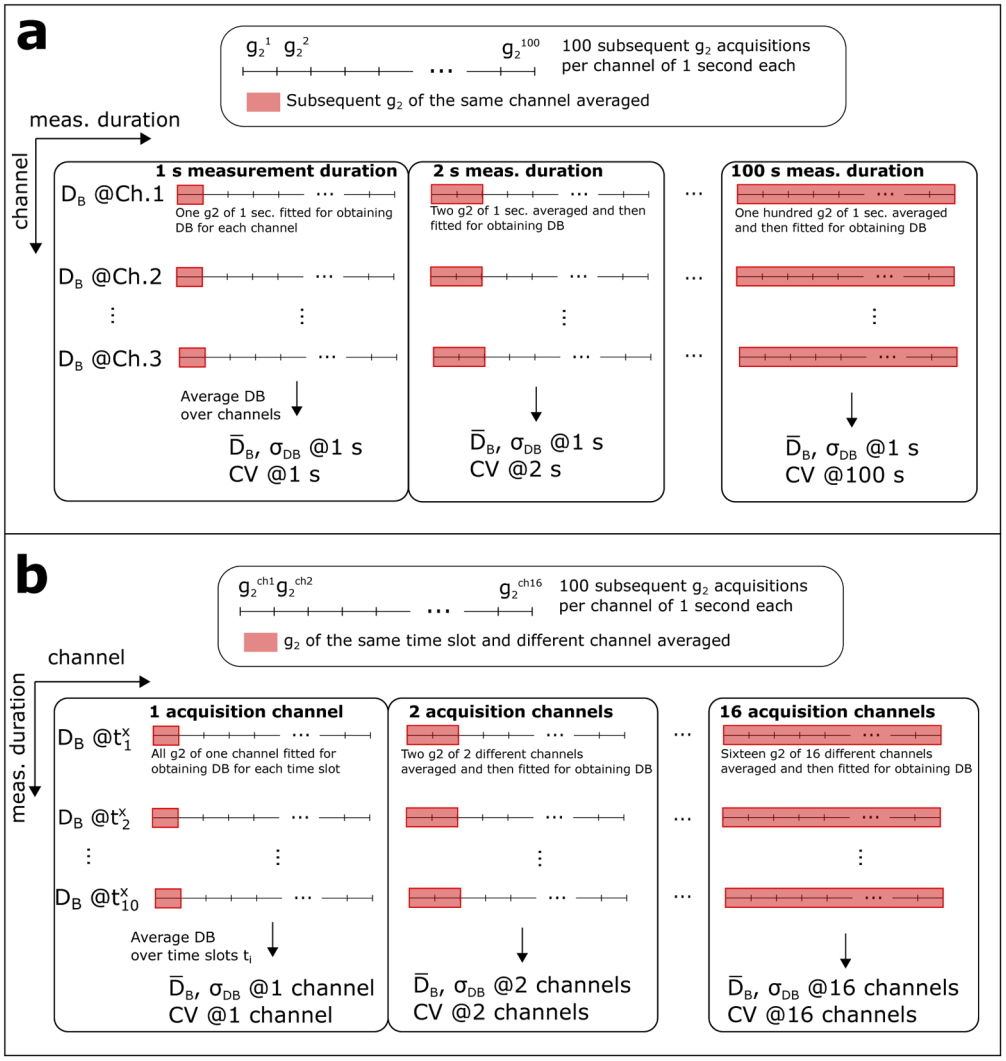

Fig. 1. Visual representation of the data analysis performed to obtain D_B variability for different measurement duration and number of detection channels, at different photon count-rates. (a) Analysis to find the dependence of the *CV* of one channel acquisitions on the measurement duration (from 1 to 100 *s*). (b) Analysis to retrieve the dependence of the *CV* on the number of detection channels for pre-determined measurement duration t^x. This analysis has been repeated considering time slots of different duration , from 1 to 10 *s* (t^{1s},. . . , t^{10s}).

Biomedical Optics EXPRESS

Finally, the average value $\overline{D}_B$ and the coefficient of variation CV have been obtained by averaging the D_B of the 10 time slots selected, and calculating the standard deviation. This procedure has been repeated for different photon count-rates and varying the temporal duration of the time slots (i.e., varying the number x of g_2 curves contained in each slot), ranging from 1 s to 10 s (t_i^{1s}, t_i^{2s},. . . , t_i^{10s}).

In summary, considering this data analysis, we have obtained a Brownian diffusion coefficient for different measurement durations (ranging from 1 to 10 s), for different number of detection channels and for different photon count-rates.

2.2.3. Noise model

The experimental results that were obtained have been compared with the theoretical noise model described in references [38,42] and derived from the model developed by Koppel et al. [59]. The standard deviation for the reduced intensity autocorrelation function $g_2(\tau) - 1$, for a multi-τ correlator architecture, is given by:

$$\sigma(\tau) = \sqrt{\frac{T}{t}}\left[\beta^2 \frac{\left(1+e^{-2\Gamma T}\right)\left(1+e^{-2\Gamma\tau}\right)+2m\left(1-e^{-2\Gamma T}\right)e^{-2\Gamma\tau}}{\left(1-e^{-2\Gamma T}\right)} + \frac{2\beta}{(IT)}\left(1+e^{-2\Gamma\tau}\right) + \frac{1}{(IT)^2}\left(1+\beta e^{-\Gamma\tau}\right)\right]^{1/2} \quad (2)$$

where t is the measurement duration, Γ is the decay rate, m is the correlator bin index related to the delay time τ, I is the detected photon count-rate, T is the correlator bin time interval (depending on the delay time τ). Considering the parameters of our DCS experiments (i.e., count-rate between 1 and 150 kHz and $\Gamma T << 1$), Eq. (2) can be simplified to [45]:

$$\sigma(\tau) \approx \frac{1}{I} \cdot \frac{1}{\sqrt{t}} \cdot \sqrt{\frac{\left(1+\beta e^{-\Gamma\tau}\right)}{T}}, \quad (3)$$

stating that the variability of the $g_2(\tau)$ scales as the inverse of the photon intensity count-rate and as inverse of the square root of the measurement. Please note that the single acquisition integration time t_{int} is a fixed experimental parameter in our experiments ($t_{int} = 1$ s), and the dependence of the precision on the measurement duration has been obtained by averaging subsequently acquired g_2 curves.

As described before, when considering the variability over the number of detection channels and over the measurement duration, we have calculated the average and standard deviation over a sample of $M = 10$ measurements. Each of the M measurements have been obtained by averaging a number N of correlation curves (with N number of detection channels or number of considered measurement duration slots of 1 second). In this situation, the standard deviation scales as the inverse of square root of N (number of the sample population) [38]. In summary, considering the approximation reported in Eq. (3), we can assume the following proportionality relation between the standard deviation $\sigma(\tau)$, the measurement duration t, the intensity I and the number of detection channels N_{CH}:

$$\sigma(\tau) \propto \frac{1}{I} \cdot \frac{1}{\sqrt{t}} \cdot \frac{1}{\sqrt{N_{CH}}}. \quad (4)$$

3. Results and discussion

Examples of the results of the calculated coefficient of variations (CV) obtained under different experimental conditions are reported in Fig. 2. In subplot (a) we show the CV for varying measurement duration (from 1 to 100 s) at different photon count-rates (from 5 to 150 kHz) when considering one detection channel (a single speckle detected). After an initial rapid decrease as the measurement duration increases, CV decreases slowly and stabilizes for longer time. In addition, as expected, the precision of the DCS measurement increases as the count-rate increases,

Biomedical Optics EXPRESS

ranging from ~ 10% (at 5 *kHz* count-rate) to <1% (at 150 *kHz*) for long measurement duration. The subplots (b), (c), and (d) of Fig. 2 show the precision of DCS measured by considering exemplary parameters, i.e., 20 *kHz* count-rate, 8 detection channels, and 1 *s* measurement duration respectively for varying measurement duration, count-rate and number of acquisition channels. The data reported show an increase of the quality as the measurement duration, number of channels and count-rate increase, with a rapid initial decrease of the *CV*, and a subsequent slower decrease.

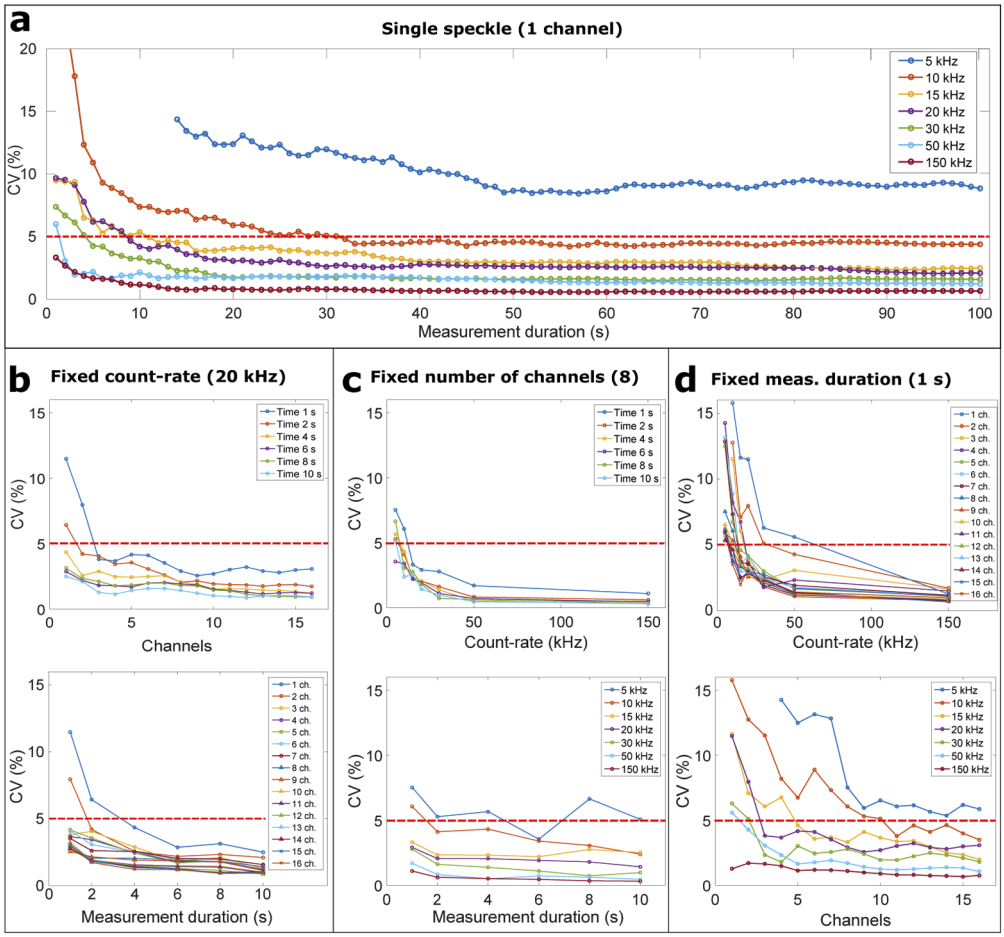

Fig. 2. Calculated *CV* for different measurement conditions. (a) *CV* for one detection channel for varying measurement duration, at different count-rates. (b) *CV* at a fixed count-rate (20 *kHz*) for varying measurement duration and number of detection channels. (c) *CV* at a fixed number of detection channels (eight) for varying measurement duration and count-rate. (d) *CV* at a fixed measurement duration (1 *s*) for varying count-rate and number of detection channels. Red dotted horizontal lines representing $CV = 5\%$ highlight a quality threshold for the precision of DCS measurements.

Together with the results, in Fig. 2 we have plotted red dotted horizontal lines, at $CV = 5\%$, to better visualize that we consider an acceptable threshold for the precision of DCS measurements. We state that this threshold is indicative and has not to be intended as a hard limit, but should help the reader in visualizing our results in light of a precision target suitable for many *in vivo* applications. Indeed, in several clinical application of DCS, 5% variability in D_B determination

Biomedical Optics EXPRESS

is well sufficient to discriminate alteration of tissue hemodynamics, for example to individuate the contrast between malignant and benign lesions and monitor the effects of neoadjuvant cancer therapies [16,60], to detect changes in the brain during sensorimotor activation [7], to monitor premature infant brain hemodynamics [12] or to monitor muscle blood flow during exercise [19].

To give an idea of the practical interpretations of the data reported in Fig. 2, we now consider few exemplary and concrete situations. For a 5% variability (precision) in a DCS experiment with a single detection channel system and a detected photon count-rate of 10 kHz, we will have to set a measurement duration of approximately 25 seconds, which, in turn, sets the maximum temporal resolution of the measurement. While when the count-rate is 20 kHz, it will be sufficient to have a measurement duration of approximately 10 seconds. On the other hand, when we have to perform an experiment with a fixed temporal resolution of one second and if the expected photon count-rate is 10 kHz, then we will have to design a DCS system with more than eight independent detection channels to achieve the target of 5% precision. If the count-rate increases to roughly 20 kHz, the minimum required number of independent detection channels will be two. Finally, for a fixed measurement time of one second and one detection channel, the precision target of 5% is reached only for detected photon count-rates higher than 50 kHz.

We conclude this list of examples by briefly commenting on the recent advancements on fast DCS acquisition at rates of $10-200$ Hz (corresponding to $5-100$ ms measurement duration) using software [46] and hardware correlators [61]. Although it is beyond the scope of this study to look at this aspect in details, the scaling relationships between the measurement duration and the number of detection channels hold here and should be utilized to evaluate the expectations in this scenario. If the goal is to observe the pulsatility index due to the cardiac cycle, where the changes in the DCS measures are shown to be larger than 100% of the diastolic value [38,62,63], then large uncertainties (e.g., >5%) can be tolerated. In this respect we note that Wang et al. [46] were able to observe heart pulsation in the DCS signal for acquisitions rate in the range $10-200$ Hz, with a system with eight detection channels and detected photon count-rate between 50 kHz and 100 kHz which falls within the expectations of this work.

In order to compare our data with the theoretical model, we have plotted the logarithm of the coefficient of variation with respect of the logarithm of our parameter of interest, i.e., measurement duration, count-rate and number of detection channels. As reported in the previous section, the theoretical model (Eq. (4)) predicts that the precision of DCS acquisitions scales with a power law, with exponent $-1/2$ when considering the dependence on the measurement duration and number of channels, and with an exponent of -1 when considering the dependence on the photon count-rate.

In Fig. 3(a) we report the coefficient of variation of the fitted D_B considering 1 detection channel and varying photon count-rate (from 5 to 150 kHz) and measurement duration (from 1 to 100 s), and the results of the linear fits (in log-log scale) considering Eq. (4) (bottom plot). As expected, as the count-rate and measurement duration increase, the coefficient of variation decreases.

The curves reported in Fig. 3(a) - top panel - show a first linear decrease of CV (in log-log scale), while for larger duration, the slope of the decrease is lower. This set a threshold above which increasing the measurement duration does not lead to a significant reduction in the precision of the measurement. The graph furthermore highlights that this temporal threshold depends on the photon count-rate, i.e., for higher count-rates the threshold occurs earlier in time. This suggests that the precision is limited by an intrinsic variability due to the phantom properties, experimental and environmental conditions, that cannot be avoided by increasing the measurement duration.

The variability of the retrieved D_B for different count-rates is highlighted by the middle panel graph of Fig. 3, showing a linear (in log-log scale) decrease of the retrieved CV as the detected photon count-rate increases, with a reduction of the slope when considering high count-rates. This reduction results evident in the bottom panel, where we report the results of the linear fits

Biomedical Optics EXPRESS

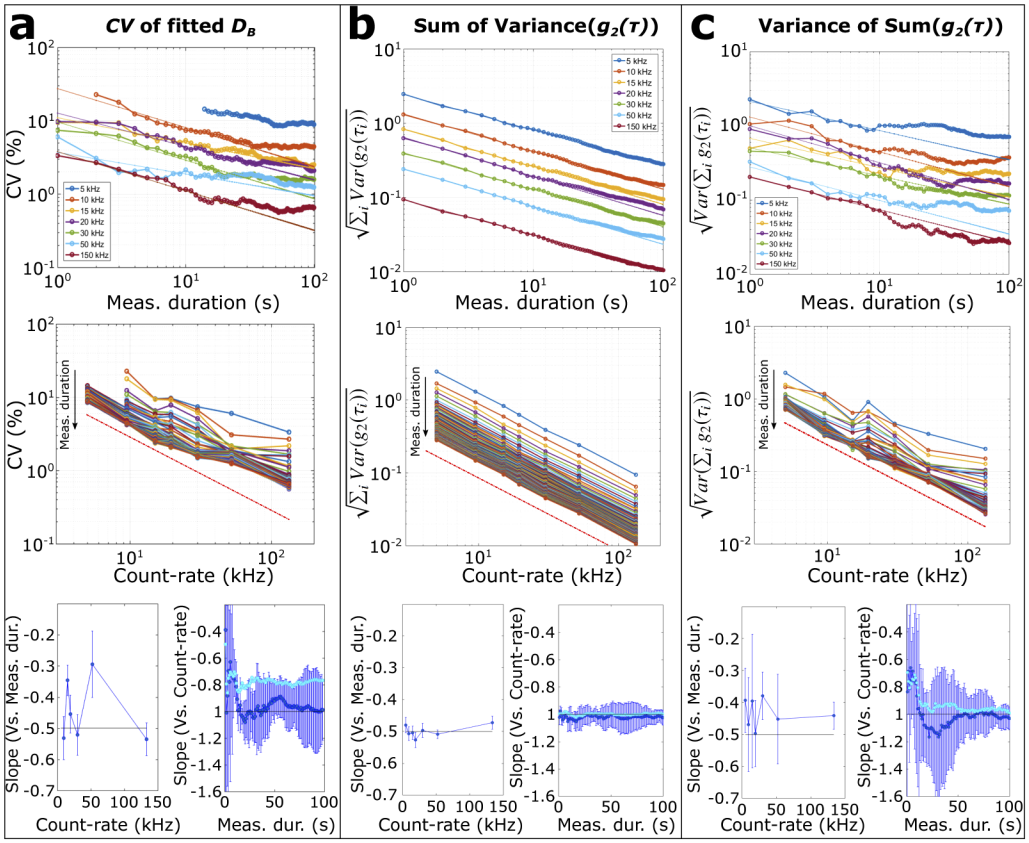

Fig. 3. Block (a): *CV* of the fitted D_B for one channel acquisitions (the *CV* is calculated by averaging the D_B obtained for all the different acquisition channels). Top panel: *CV* for varying measurement duration at different count-rates. The dotted lines represent the fits of the first part of the curves. Middle panel: *CV* for varying count-rate at different measurement duration (different colors represent different measurement durations). The red dotted line represents the expectations from theory (only the slope is indicative, see Eq. (3)). Bottom panel: Results of the fitted slopes of the lines in top and bottom panel, and comparison with theory (i.e., slope -0.5 for $log(CV)$ Vs. $log(Meas.\ dur.)$, and slope -1 for $log(CV)$ Vs. $log(Count-rate)$); light blue points represent results of fit considering all the count-rates investigated, dark blue points with errorbar represent the results of the fit excluding high count-rate acquisitions (i.e., 50 and 150 *kHz*). Block (b): Same of block (a) but considering the square root of the sum of the variances of g_2 at every single τ bin ($\sqrt{\sum_i Var(g_2(\tau_i))}$). Block (c): Same of block (a) but considering the square root of the variance (i.e., the standard deviation) of the sum of g_2 at every single τ bin ($\sqrt{Var(\sum_i g_2(\tau_i))}$).

Biomedical Optics EXPRESS

(in log-log scale) of the curves reported in the top and middle panels. Here, the slopes measured by considering only the lower count-rates (up to 30 *kHz*) are significantly smaller than the slopes measured by considering all the count-rates.

At this point, it is necessary to note that the comparison of our results with the theoretical model is not trivial, and some further considerations are needed. The curves reported in Fig. 3(a) are indeed quite noisy, and the time and intensity dependencies are not clear. We note here that the theory reported in Eqs. (2), (3) and (4) describes the noise associated to each temporal bin τ of the correlator, while the noise related to the measured D_B is representative of the collective effect due to the noise of the g_2 at all the τ considered for the fitting procedure [64–66].

To highlight the impact of the collective effects of the noise of each correlator bin, we have plotted the same graphs reported in block (a) of Fig. 3 but considering the square root of the sum of the variance of the g_2 at each τ ($\sqrt{\sum_i Var(g_2(\tau_i))}$, block (b)) and the square root of the variance (i.e., the standard deviation) of the sum of all the value of $g_2(\tau)$ for all the τ bins (up to $\tau = 1/\Gamma$) considered for retrieving the D_B ($\sqrt{Var(\sum_i g_2(\tau_i))}$, block (c)). We note here that these two quantities are related through the formula

$$Var(\sum_i g_2(\tau_i)) = \sum_i Var(g_2(\tau_i)) + \sum_{i \neq j} Cov(g_2(\tau_i), g_2(\tau_j)), \tag{5}$$

where $Var(g_2(\tau_i))$ represents the diagonal elements of the covariance matrix, while $Cov(g_2(\tau_i), g_2(\tau_j))$ with $i \neq j$ the non diagonal elements, that account for the correlations between noise at different correlator bins. In case the acquisitions at different bins are independent (that is not the case of the measurements reported in this paper), the non diagonal elements of the covariance matrix are equal to zero.

The plots reported in block (b) (top and middle panel) and the results of the linear fits (in log-log scale), reported in the bottom panel, highlight the clear agreement of our results and the theory represented by Eq. (3), when considering the square root of the sum of the variance of the g_2 at each τ. In the case we consider the square root of the variance of the sum of all the value of $g_2(\tau)$ (block (c)), the plots reported show a very similar behavior to what reported for the *CV* of the fitted D_B (block (a)). This because the retrieved D_B depends on the whole g_2 curve and, consequently, its precision depends also on the correlation between the noise in different τ bins. This behavior is described by the theory developed by Schätzel in ref. [64] and revised by Biganzoli and Ferri in [65], who have described the detected noise in the photon autocorrelation measurements considering a single exponential decay autocorrelation function model.

In light of this theoretical model, we note that the non-diagonal covariance matrix elements for the g_2 between different delay time bins, describing the correlation between the noise of different bins, become important as the count-rate increases due to the intrinsic nature of photon detection and correlator architecture, limiting the decrease of the noise and causing a deviation with respect to Eq. (4), while, at a fixed count-rate, the temporal dependence of the variance shows no significant deviation with the above formula [65].

In this respect, while the difference between block (b) and (c) for the intensity dependence (graphs in the middle) are partially due to intrinsic calculation and detection noise, the differences for the temporal dependence (top graphs) are essentially to be ascribed to environmental conditions and fluctuations during the experiment. We also note here, that the environmental conditions mainly affect the non-diagonal elements of the covariance matrix between the different correlator τ bins (see Eq. (5)), generating fluctuations, as evident looking at the differences between blocks (b) and (c) of Fig. 3. All these effects impact on the retrieval of the noise of the fitted Brownian diffusion coefficient D_B, as reported in block (a).

We also note that the differences between block (a) and (b) of Fig. 3 can be partially ascribed to the minimization algorithm that is commonly used for the fitting process. In this regard we note that recent studies are proposing new methods to retrieve the D_B aiming to reduce the variability

Biomedical Optics EXPRESS

common of non-linear fitting processes [67–70]. These approaches do not change the scaling relationships that are described in this manuscript.

The same experimental data that were used to produce Fig. 3 have been analyzed in order to retrieve information about the precision of the measurements for a varying number of detection channels and measurement duration (1 to 10 s) at a fixed count-rate, for varying count-rates and measurement durations at a fixed number of detection channels, and for varying count-rates and number of detection channels at a fixed measurement duration. In Fig. 4, we report examples for (a) count-rate = 20 kHz, (b) 8 detection channels and (c) 1 s measurement duration, together with expectation from the theory (red line, only the slope is indicative). All the curves reported in Fig. 4 show a linear decrease of CV with respect to the correspondent parameter in log-log scale in qualitative accordance with Eq. (4), which predicts a decay in linear scale with a power law with exponent $-1/2$ when considering the dependence on the measurement duration and number of channels, and with an exponent of -1 when considering the dependence on the photon count-rate.

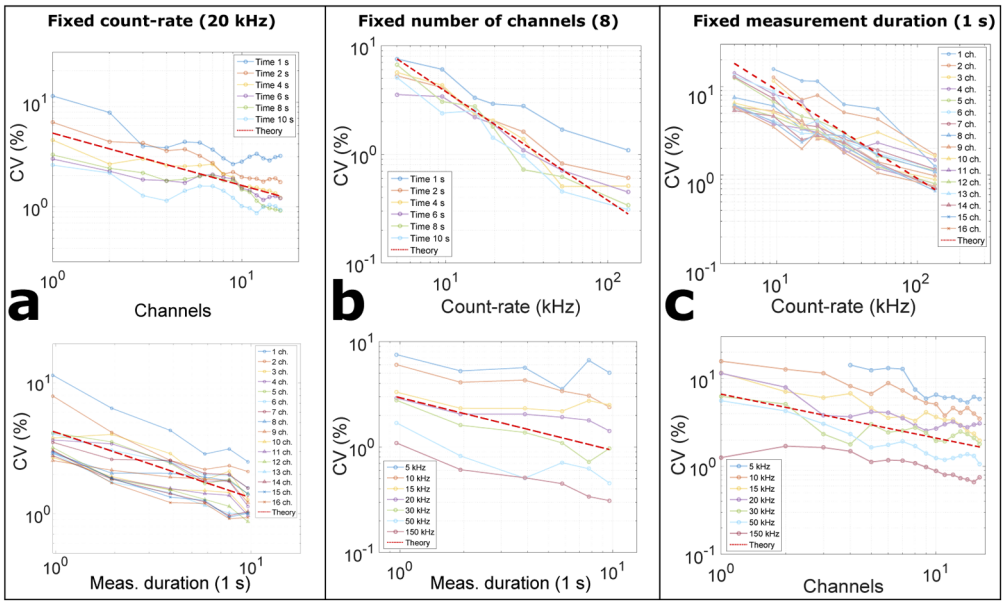

Fig. 4. Examples of calculated coefficient of variation CV at fixed (a) count-rate (20 kHz) (top: CV Vs. number of detection channels, bottom: CV Vs. measurement duration), (b) number of detection channels (8) (top: CV Vs. count-rate, bottom: CV Vs. measurement duration) and (c) measurement duration (1 s) (top: CV Vs. count-rate, bottom: CV Vs. number of detection channels).

These data have been plotted, with a three dimensional representation, in Fig. 5, together with the linear surface fits performed. The results of all the linear (in log-log scale) surface fits for all the values of count-rate, number of detection channel and measurement duration have been reported in the right panel of the same figure. Again, the results qualitatively reproduce the scaling relation reported in Eq. (4).

Biomedical Optics EXPRESS

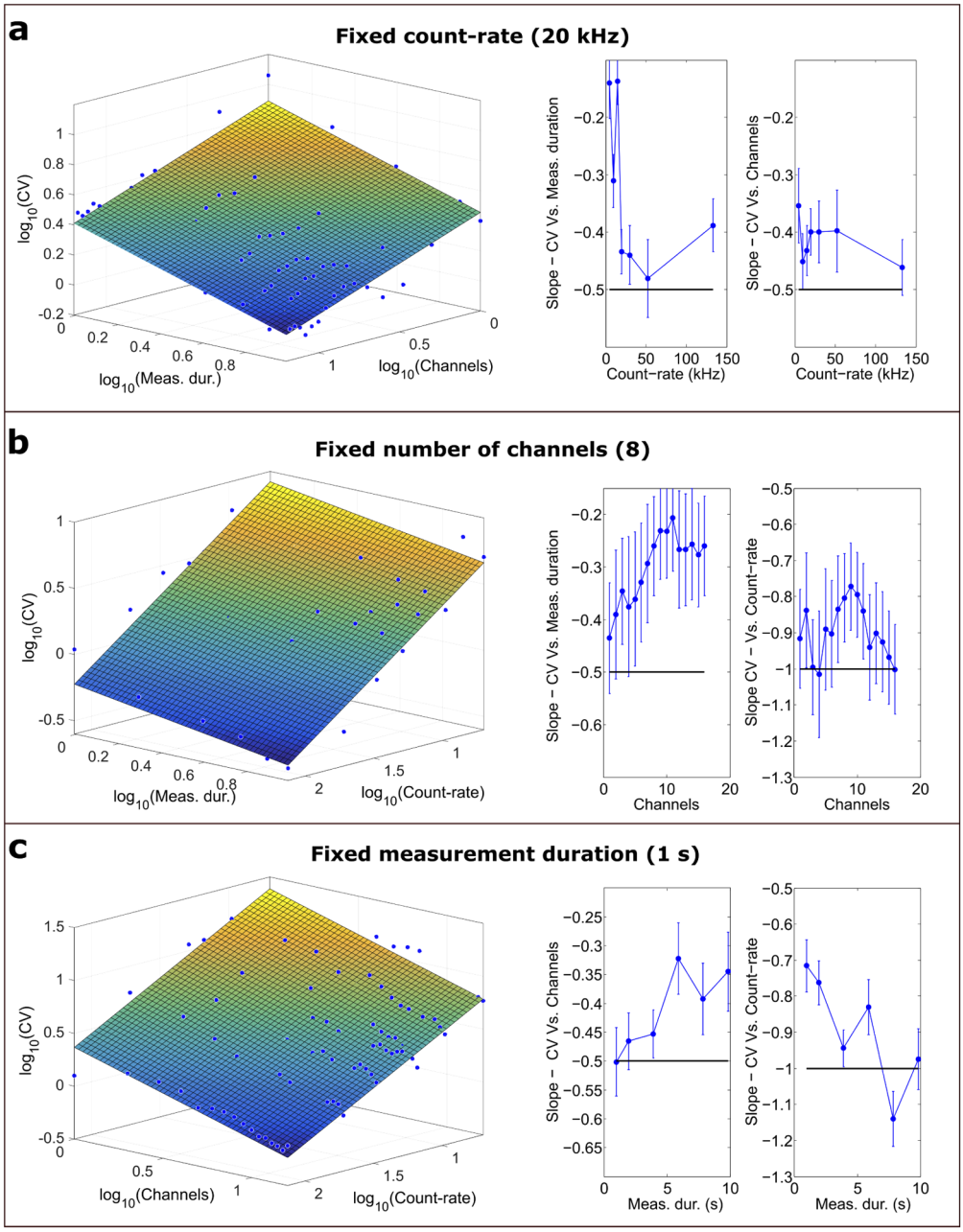

Fig. 5. (a) Left: 3D representation and surface linear fit of measured *CV* at a fixed count-rate (20 *kHz*) for varying number of detection channels and measurement duration. Right: Result of the correspondent fits (slopes along measurement duration axis and number of detection channel axis) for all the count-rates investigated (5 to 150 *kHz*). The black horizontal lines represent the expectation from the theory (Eq. (3)). (b) Left: 3D representation and surface linear fit of measured *CV* at a fixed number of detection channels (8 channels) for varying count-rate and measurement duration. Right: Result of the correspondent fit (slopes along measurement duration axis and count-rate axis) for all the detection channel considered (1 to 16). (c) Left: 3D representation and surface linear fit of measured *CV* at a fixed measurement duration (1 *s*) for varying number of detection channels and count-rate. Right: Result of the correspondent fit (slopes along count-rate axis and number of detection channel axis) for all the measurement durations considered (1 to 10 *s*).

Biomedical Optics EXPRESS

4. Conclusion

In this paper, we have presented a systematic phantom study on the precision of DCS measurements. We have identified the detected photon count-rate, the measurement duration and the number of independent acquisition channels as key parameters that can be controlled to obtain high quality measurements. We have, then, determined the coefficient of variation CV of the measured D_B at different values of these parameters. The results are in qualitative agreement with the theoretical model, which states that the precision of DCS acquisitions scales with a power law, with exponent $-1/2$ when considering the dependence on the measurement duration and number of channels, and with an exponent of -1 when considering the dependence on the photon count-rate. In some cases, we have reported an underestimation of the slope of the decrease of the coefficient of variation. This underestimation has to be ascribed to sub-optimal experimental and environmental condition and to collective effects between the noise of $g_2(\tau)$ recorded at different delay times τ, as described in references [64–66].

The study reported has focused on "canonical" DCS instrumentation describing how typical hardware and experimental parameters affect the precision of the DCS measurements. The approach used here to investigate the DCS precision could in future be extended to other several important factors that are not directly analyzed in this study. These are linked to more recent DCS advancements in hardware and processing methods. For completeness, we cite here new correlators and correlator designs to perform fast DCS acquisition [46,61], the use of laser sources with different wavelengths combined with new detectors [32,33], the use of a few mode instead of single mode fibers in detection [51], and of different data analysis/fitting procedures [69,70]. Furthermore, as mentioned in the Introduction, there are also recent advances in the use of more advanced physical concepts and data-types that have not been studied here. Nevertheless, the recipes that are described here can be utilized as a starting point to evaluate different approaches. We also note that multi-wavelength DCS systems have been proposed to utilize DCS hardware in a fashion analogous to continuous wave near-infrared spectroscopy to obtain estimates of the changes in hemoglobin concentrations [51,71,72]. The recipes described herein are applicable to those wavelengths.

We also note that we did not evaluate the trueness of DCS measurements, in other words, we did not provide a recipe to obtain the true values of the quantities of interest. This is mainly due to the limitations of the field. Unfortunately, to date, methods for robust, independent measurement of the quantities of interest has not been devised. This would be a topic for future investigation.

Finally, we did not explicitly evaluate the ability to follow temporal variations with DCS, as is often done for bed-site neuro-monitoring [5]. This depends on various other factors such as post-processing (e.g., temporal filtering), the frequency components of the variations and the interactions of these parameters with the type of factors discussed in this manuscript. Instead, we state that the models that describe noise and signal in DCS [38,41–43] can be utilized with the recipes describe herein to derive estimates in combination with the desired post-processing steps as well as the nature of the signals.

In conclusion, the results obtained in this study provide simple recipes to optimize the measurement settings (i.e., duration of the acquisition) and hardware design (i.e., number of necessary detection channels) for different DCS measurement conditions. Furthermore, by extending the results to different scatterer dynamics (for example by analyzing the precision in phantoms with different viscosities), can be opened the way to implement *data driven*, real-time automatized algorithm that can tune the acquisition settings to obtain the desired precision.

Funding. Horizon 2020 Framework Programme (101016087, 101017113, 675332, 688303); Fundación Cellex; Fundació Mir-Puig; Agencia Estatal de Investigación (PHOTOMETABO, PID2019-106481RB-C31/10.13039/501100011033); "Severo Ochoa" Programme for Centres of Excellence in R&D (CEX2019-000910-S); "la Caixa" Foundation (LlumMed-Bcn); Generalitat de Catalunya (AGAUR-2017-SGR-1380, CERCA, RIS3CAT-001-P-001682 CECH); FEDER EC; Laserlab-Europe.

Biomedical Optics EXPRESS

Acknowledgments. This work has received funding from the European Union's Horizon 2020 research and innovation programme under grant agreements No. 688303 (LUCA), No. 101016087 (VASCOVID), No. 101017113 (TINYBRAINS), No. 675332 (BITMAP). Fundació CELLEX Barcelona, Fundació Mir-Puig, Agencia Estatal de Investigación (PHOTOMETABO, PID2019-106481RB-C31/10.13039/501100011033), the "Severo Ochoa" Programme for Centres of Excellence in R&D (CEX2019-000910-S), the Obra social "la Caixa" Foundation (LlumMedBcn), Generalitat de Catalunya (CERCA, AGAUR-2017-SGR-1380, RIS3CAT-001-P-001682 CECH), FEDER EC and LASERLAB-EUROPE V (EC H2020 no. 871124).

Disclosures. The role in the project of all the companies and their employees involved has been defined by the project objectives, tasks, and work packages and has been reviewed by the European Commission (grant agreement No. 688303, LUCA-project). Turgut Durduran is an inventor of a relevant patent (Patent US8082015B2). ICFO has equity ownership in the spin-off company HemoPhotonics S.L.. Udo Weigel is the CEO, has equity ownership and is an employee of the company. The potential financial conflicts of interest and objectivity of research have been monitored by ICFO's Knowledge & Technology Transfer Department and none were identified. Davide Contini and Alberto Dalla Mora are co-founders of pioNIRS s.r.l., spin-off company from Politecnico di Milano (POLIMI, Italy). Their potential financial conflicts of interest and the objectivity of research has been monitored by POLIMI and none were identified.

References

1. D. A. Boas, L. E. Campbell, and A. G. Yodh, "Scattering and imaging with diffusing temporal field correlations," Phys. Rev. Lett. **75**(9), 1855–1858 (1995).
2. D. A. Boas and A. G. Yodh, "Spatially varying dynamical properties of turbid media probed with diffusing temporal light correlation," J. Opt. Soc. Am. A **14**(1), 192 (1997).
3. T. Durduran, R. Choe, W. B. Baker, and A. G. Yodh, "Diffuse optics for tissue monitoring and tomography," Rep. Prog. Phys. **73**(7), 076701 (2010).
4. G. Yu, "Diffuse correlation spectroscopy (DCS): a diagnostic tool for assessing tissue blood flow in vascular-related diseases and therapies," Curr. Med. Imaging Rev. **8**(3), 194–210 (2012).
5. T. Durduran and A. G. Yodh, "Diffuse correlation spectroscopy for non-invasive, micro-vascular cerebral blood flow measurement," NeuroImage **85**, 51–63 (2014).
6. E. M. Buckley, A. B. Parthasarathy, P. E. Grant, A. G. Yodh, and M. A. Franceschini, "Diffuse correlation spectroscopy for measurement of cerebral blood flow: future prospects," Neurophotonics **1**(1), 011009 (2014).
7. T. Durduran, G. Yu, M. G. Burnett, J. A. Detre, J. H. Greenberg, J. Wang, C. Zhou, and A. G. Yodh, "Diffuse optical measurement of blood flow, blood oxygenation, and metabolism in a human brain during sensorimotor cortex activation," Opt. Lett. **29**(15), 1766–1768 (2004).
8. J. Li, G. Dietsche, D. Iftime, S. E. Skipetrov, G. Maret, T. Elbert, B. Rockstroh, and T. Gisler, "Noninvasive detection of functional brain activity with near-infrared diffusing-wave spectroscopy," J. Biomed. Opt. **10**(4), 044002 (2005).
9. N. Roche-Labarbe, A. Fenoglio, H. Radhakrishnan, M. Kocienski-Filip, S. A. Carp, J. Dubb, D. A. Boas, P. E. Grant, and M. A. Franceschini, "Somatosensory evoked changes in cerebral oxygen consumption measured non-invasively in premature neonates," NeuroImage **85**, 279–286 (2014).
10. B. Andresen, A. C. De, M. Fumagalli, M. Giovannella, T. Durduran, U. W. Michael, D. Contini, L. Spinelli, A. Torricelli, and G. Greisen, "Cerebral oxygenation and blood flow in normal term infants at rest measured by a hybrid near-infrared device (babylux)," Pediatric Res. **86**(4), 515–521 (2019).
11. M. Diop, J. Kishimoto, V. Toronov, D. S. Lee, and K. S. Lawrence, "Development of a combined broadband near-infrared and diffusion correlation system for monitoring cerebral blood flow and oxidative metabolism in preterm infants," Biomed. Opt. Express **6**(10), 3907–3918 (2015).
12. N. Roche-Labarbe, S. A. Carp, A. Surova, M. Patel, D. A. Boas, P. E. Grant, and M. A. Franceschini, "Noninvasive optical measures of CBV, StO2, CBF index, and rCMRO2 in human premature neonates' brains in the first six weeks of life," Hum. Brain Mapp. **31**, 341–352 (2010).
13. C. Gregori-Pla, I. Blanco, P. Camps-Renom, P. Zirak, I. Serra, G. Cotta, F. Maruccia, L. Prats-Sánchez, A. Martínez-Domeño, D. R. Busch, G. Giacalone, J. Martí-Fábregas, T. Durduran, and R. Delgado-Mederos, "Early microvascular cerebral blood flow response to head-of-bed elevation is related to outcome in acute ischemic stroke," J. Neurol. **266**(4), 990–997 (2019).
14. T. Durduran, R. Choe, G. Yu, C. Zhou, J. C. Tchou, B. J. Czerniecki, and A. G. Yodh, "Diffuse optical measurement of blood flow in breast tumors," Opt. Lett. **30**(21), 2915–2917 (2005).
15. R. Choe and T. Durduran, "Diffuse optical monitoring of the neoadjuvant breast cancer therapy," IEEE J. Sel. Top. Quantum Electron. **18**(4), 1367–1386 (2012).
16. J. Cochran, S. Chung, A. Leproux, W. Baker, D. Busch, A. DeMichele, J. Tchou, B. Tromberg, and A. Yodh, "Longitudinal optical monitoring of blood flow in breast tumors during neoadjuvant chemotherapy," Phys. Med. Biol. **62**(12), 4637–4653 (2017).
17. C. Lindner, M. Mora, P. Farzam, M. Squarcia, J. Johansson, U. M. Weigel, I. Halperin, F. A. Hanzu, and T. Durduran, "Diffuse Optical Characterization of the Healthy Human Thyroid Tissue and Two Pathological Case Studies," PLoS One **11**(1), e0147851 (2016).
18. K. Gurley, Y. Shang, and G. Yu, "Noninvasive optical quantification of absolute blood flow, blood oxygenation, and oxygen consumption rate in exercising skeletal muscle," J. Biomed. Opt. **17**(7), 0750101 (2012).

Biomedical Optics EXPRESS

19. V. Quaresima, P. Farzam, P. Anderson, P. Y. Farzam, D. Wiese, S. A. Carp, M. Ferrari, and M. A. Franceschini, "Diffuse correlation spectroscopy and frequency-domain near-infrared spectroscopy for measuring microvascular blood flow in dynamically exercising human muscles," J. Appl. Physiol. **127**(5), 1328–1337 (2019).
20. T. S. Ko, C. D. Mavroudis, W. B. Baker, V. C. Morano, K. Mensah-Brown, T. W. Boorady, A. L. Schmidt, J. M. Lynch, D. R. Busch, J. Gentile, G. Bratinov, Y. Lin, S. Jeong, R. W. Melchior, T. M. Rosenthal, B. C. Shade, K. L. Schiavo, R. Xiao, J. W. Gaynor, A. G. Yodh, T. J. Kilbaugh, and D. J. Licht, "Non-invasive optical neuromonitoring of the temperature-dependence of cerebral oxygen metabolism during deep hypothermic cardiopulmonary bypass in neonatal swine," J. Cereb. Blood Flow Metab. **40**(1), 187–203 (2020).
21. Y. Shang, R. Cheng, L. Dong, S. J. Ryan, S. P. Saha, and G. Yu, "Cerebral monitoring during carotid endarterectomy using near-infrared diffuse optical spectroscopies and electroencephalogram," Phys. Med. Biol. **56**(10), 3015–3032 (2011).
22. D. R. Busch, W. Lin, C. Cai, A. Cutrone, J. Tatka, B. J. Kovarovic, A. G. Yodh, T. F. Floyd, and J. Barsi, "Multi-site optical monitoring of spinal cord ischemia during spine distraction," J. Neurotrauma **37**(18), 2014–2022 (2020). PMID: 32458719.
23. Standard ISO 5725-1:1994, International Organization for Standardization.
24. Wikipedia contributors, "Accuracy and precision — Wikipedia, the free encyclopedia," https://en.wikipedia.org/wiki/Accuracy_and_precision (2021).
25. R. Bi, J. Dong, and K. Lee, "Deep tissue flowmetry based on diffuse speckle contrast analysis," Opt. Lett. **38**(9), 1401–1403 (2013).
26. C. P. Valdes, H. M. Varma, A. K. Kristoffersen, T. Dragojevic, J. P. Culver, and T. Durduran, "Speckle contrast optical spectroscopy, a non-invasive, diffuse optical method for measuring microvascular blood flow in tissue," Biomed. Opt. Express **5**(8), 2769–2784 (2014).
27. H. M. Varma, C. P. Valdes, A. K. Kristoffersen, J. P. Culver, and T. Durduran, "Speckle contrast optical tomography: A new method for deep tissue three-dimensional tomography of blood flow," Biomed. Opt. Express **5**(4), 1275–1289 (2014).
28. C. Huang, D. Irwin, Y. Lin, Y. Shang, L. He, W. Kong, J. Luo, and G. Yu, "Speckle contrast diffuse correlation tomography of complex turbid medium flow," Med. Phys. **42**(7), 4000–4006 (2015).
29. K. Zarychta, E. Tinet, L. Azizi, S. Avrillier, D. Ettori, and J.-M. Tualle, "Time-resolved diffusing wave spectroscopy with a ccd camera," Opt. Express **18**(16), 16289–16301 (2010).
30. W. Zhou, O. Kholiqov, S. P. Chong, and V. J. Srinivasan, "Highly parallel, interferometric diffusing wave spectroscopy for monitoring cerebral blood flow dynamics," Optica **5**(5), 518–527 (2018).
31. M. B. Robinson, D. A. Boas, S. Sakadžic, M. A. Franceschini, and S. A. Carp, "Interferometric diffuse correlation spectroscopy improves measurements at long source–detector separation and low photon count rate," J. Biomed. Opt. **25**(9), 097004 (2020).
32. S. A. Carp, D. Tamborini, D. Mazumder, K.-C. Wu, M. B. Robinson, K. A. Stephens, O. Shatrovoy, N. Lue, N. Ozana, M. H. Blackwell, and M. A. Franceschini, "Diffuse correlation spectroscopy measurements of blood flow using 1064 nm light," J. Biomed. Opt. **25**(9), 097003 (2020).
33. L. Colombo, M. Pagliazzi, S. K. V. Sekar, D. Contini, T. Durduran, and A. Pifferi, "In vivo time-domain diffuse correlation spectroscopy above the water absorption peak," Opt. Lett. **45**(13), 3377–3380 (2020).
34. J. Sutin, B. Zimmerman, D. Tyulmankov, D. Tamborini, K. C. Wu, J. Selb, A. Gulinatti, I. Rech, A. Tosi, D. A. Boas, and M. A. Franceschini, "Time-domain diffuse correlation spectroscopy," Optica **3**(9), 1006–1013 (2016).
35. M. Pagliazzi, S. K. V. Sekar, L. Colombo, E. Martinenghi, J. Minnema, R. Erdmann, D. Contini, A. D. Mora, A. Torricelli, A. Pifferi, and T. Durduran, "Time domain diffuse correlation spectroscopy with a high coherence pulsed source: in vivo and phantom results," Biomed. Opt. Express **8**(11), 5311–5325 (2017).
36. M. Pagliazzi, S. K. V. Sekar, L. Di Sieno, L. Colombo, T. Durduran, D. Contini, A. Torricelli, A. Pifferi, and A. Dalla Mora, "In vivo time-gated diffuse correlation spectroscopy at quasi-null source-detector separation," Opt. Lett. **43**(11), 2450–2453 (2018).
37. J. Xu, A. K. Jahromi, and C. Yang, "Diffusing wave spectroscopy: a unified treatment on temporal sampling and speckle ensemble methods," arXiv p. 2010.13979 (2020).
38. G. Dietsche, M. Ninck, C. Ortolf, J. Li, F. Jaillon, and T. Gisler, "Fiber-based multispeckle detection for time-resolved diffusing-wave spectroscopy: characterization and application to blood flow detection in deep tissue," Appl. Opt. **46**(35), 8506 (2007).
39. D. Irwin, L. Dong, Y. Shang, R. Cheng, M. Kudrimoti, S. D. Stevens, and G. Yu, "Influences of tissue absorption and scattering on diffuse correlation spectroscopy blood flow measurements," Biomed. Opt. Express **2**(7), 1969 (2011).
40. L. D. Sieno, D. Contini, G. L. Presti, L. Cortese, T. Mateo, B. Rosinski, E. Venturini, P. Panizza, M. Mora, G. Aranda, M. Squarcia, A. Farina, T. Durduran, P. Taroni, A. Pifferi, and A. D. Mora, "Systematic study of the effect of ultrasound gel on the performances of time-domain diffuse optics and diffuse correlation spectroscopy," Biomed. Opt. Express **10**(8), 3899–3915 (2019).
41. W. Brown, *Dynamic Light Scattering: The Method and Some Applications*, vol. 49 (Oxford University Press, 1993).
42. C. Zhou, G. Yu, D. Furuya, J. H. Greenberg, A. G. Yodh, and T. Durduran, "Diffuse optical correlation tomography of cerebral blood flow during cortical spreading depression in rat brain," Opt. Express **14**(3), 1125–1144 (2006).
43. D. Wang, P. Gao, L. Zhu, Q. Peng, Z. Li, and J. Zhao, "Optimization of detected optical intensity for measurement of diffuse correlation spectroscopy: Intralipid phantom study," AIP Adv. **9**(1), 015315 (2019).

Biomedical Optics EXPRESS

44. Y. Zhang, L. Huang, N. Zhang, H. Tian, and J. Zhu, "Experimental study on the sensitive depth of backwards detected light in turbid media," Opt. Express **26**(11), 14700–14709 (2018).
45. C. Zhou, *In-vivo Optical Imaging and Spectroscopy of Cerebral Hemodynamics* (University of Pennsylvania, 2007).
46. D. Wang, A. B. Parthasarathy, W. B. Baker, K. Gannon, V. Kavuri, T. Ko, S. Schenkel, Z. Li, Z. Li, M. T. Mullen, J. A. Detre, and A. G. Yodh, "Fast blood flow monitoring in deep tissues with real-time software correlators," Biomed. Opt. Express **7**(3), 776–797 (2016).
47. J. Dong, R. Bi, J.-H. Ho, K. Lee, P. S. Thong, and K.-C. Soo, "Diffuse correlation spectroscopy with a fast fourier transform-based software autocorrelator," J. Biomed. Opt. **17**(9), 0970041 (2012).
48. A. Biswas, D. A. Buffone, and A. B. Parthasarathy, "Fast diffuse correlation spectroscopy with low-cost microcontroller," in *Microscopy Histopathology and Analytics*, (Optical Society of America, 2018), pp. JW3A–20.
49. M. Giovannella, "BabyLux device: a diffuse optical system integrating diffuse correlation spectroscopy and time-resolved near-infrared spectroscopy for the neuromonitoring of the premature newborn brain," Neurophotonics **6**(2), 1 (2019).
50. M. Nourhashemi, M. Mahmoudzadeh, and F. Wallois, "Thermal impact of near-infrared laser in advanced noninvasive optical brain imaging," Neurophotonics **3**(1), 015001 (2016).
51. L. He, Y. Lin, Y. Shang, B. J. Shelton, and G. Yu, "Using optical fibers with different modes to improve the signal-to-noise ratio of diffuse correlation spectroscopy flow-oximeter measurements," J. Biomed. Opt. **18**(3), 037001 (2013).
52. J. D. Johansson, D. Portaluppi, M. Buttafava, and F. Villa, "A multipixel diffuse correlation spectroscopy system based on a single photon avalanche diode array," J. Biophotonics **12**, e201900091 (2019).
53. W. Liu, R. Qian, S. Xu, P. C. Konda, M. Harfouche, D. Borycki, J. Jönsson, E. Berrocal, C. Cooke, A. Sinclair, H. Wang, Q. Dai, and R. W. Horstmeyer, "Fast and sensitive diffuse correlation spectroscopy with highly parallelized single photon detection," bioRxiv p. 2020.07.08.193433 (2020).
54. E. J. Sie, H. Chen, E.-F. Saung, R. Catoen, T. Tiecke, M. A. Chevillet, and F. Marsili, "High-sensitivity multispeckle diffuse correlation spectroscopy," Neurophotonics **7**(3), 035010 (2020).
55. L. Cortese, G. L. Presti, M. Zanoletti, G. Aranda, M. Buttafava, D. Contini, A. D. Mora, H. Dehghani, L. D. Sieno, S. de Fraguier, F. Hanzu, M. M. Porta, A. Nguyen-Dihn, M. Renna, B. Rosinski, M. Squarcia, A. Tosi, U. M. Weigel, S. Wojtkiewicz, and T. Durduran, "The LUCA device: a multi-modal platform combining diffuse optics and ultrasound imaging for thyroid cancer screening," Paper submitted (2021).
56. http://www.luca-project.eu.
57. L. Cortese, G. L. Presti, M. Pagliazzi, D. Contini, A. Dalla Mora, A. Pifferi, S. K. V. Sekar, L. Spinelli, P. Taroni, M. Zanoletti, U. M. Weigel, S. de Fraguier, A. Nguyen-Dihn, B. Rosinski, and T. Durduran, "Liquid phantoms for near-infrared and diffuse correlation spectroscopies with tunable optical and dynamic properties," Biomed. Opt. Express **9**(5), 2068 (2018).
58. J. J. Selb, D. A. Boas, S.-T. Chan, K. C. Evans, E. M. Buckley, and S. A. Carp, "Sensitivity of near-infrared spectroscopy and diffuse correlation spectroscopy to brain hemodynamics: simulations and experimental findings during hypercapnia," Neurophotonics **1**(1), 015005 (2014).
59. D. E. Koppel, "Statistical accuracy in fluorescence correlation spectroscopy," Phys. Rev. A **10**(6), 1938–1945 (1974).
60. C. Zhou, R. Choe, N. S. Shah, T. Durduran, G. Yu, A. Durkin, D. Hsiang, R. Mehta, J. A. Butler, A. E. Cerussi, B. J. Tromberg, and A. G. Yodh, "Diffuse optical monitoring of blood flow and oxygenation in human breast cancer during early stages of neoadjuvant chemotherapy," J. Biomed. Opt. **12**(5), 051903 (2007).
61. J. B. Fischer, A. Ghouse, S. Tagliabue, F. Maruccia, A. Rey-Perez, M. Báguena, P. Cano, R. Zucca, U. M. Weigel, J. Sahuquillo, M. A. Poca, and T. Durduran, "Non-invasive estimation of intracranial pressure by diffuse optics: a proof-of-concept study," J. Neurotrauma **37**(23), 2569–2579 (2020).
62. W. B. Baker, A. B. Parthasarathy, K. P. Gannon, V. C. Kavuri, D. R. Busch, K. Abramson, L. He, R. C. Mesquita, M. T. Mullen, J. A. Detre, J. H. Greenberg, D. J. Licht, R. Balu, W. A. Kofke, and A. G. Yodh, "Noninvasive optical monitoring of critical closing pressure and arteriole compliance in human subjects," J. Cereb. Blood Flow Metab. **37**(8), 2691–2705 (2017).
63. D. Wang, W. B. Baker, H. He, P. Gao, L.-G. Zhu, Q. Peng, Z.-R. Li, F. Li, T. Chen, and H. Feng, "Influence of probe pressure on the pulsatile diffuse correlation spectroscopy blood flow signal on the forearm and forehead regions," Neurophotonics **6**(3), 035013 (2019).
64. K. Schätzel, "Noise on photon correlation data. I. Autocorrelation functions," Quantum Opt. **2**(4), 287–305 (1990).
65. D. Biganzoli and F. Ferri, "Statistical analysis of dynamic light scattering data: revisiting and beyond the Schätzel formulas," Opt. Express **26**(22), 29375–29392 (2018).
66. D. Harrison and M. R. Fisch, "Experimental study of noise on photon autocorrelation functions," Langmuir **12**(26), 6691–6700 (1996).
67. Y. Shang and G. Yu, "A nth-order linear algorithm for extracting diffuse correlation spectroscopy blood flow indices in heterogeneous tissues," Appl. Phys. Lett. **105**(13), 133702 (2014).
68. P. Zhang, Z. Gui, G. Guo, and Y. Shang, "Approaches to denoise the diffuse optical signals for tissue blood flow measurement," Biomed. Opt. Express **9**(12), 6170–6185 (2018).
69. P. Zhang, Z. Gui, L. Hao, X. Zhang, C. Liu, and Y. Shang, "Signal processing for diffuse correlation spectroscopy with recurrent neural network of deep learning," in *2019 IEEE Fifth International Conference on Big Data Computing Service and Applications (BigDataService)*, (IEEE, 2019), pp. 328–332.

Biomedical Optics EXPRESS

70. M. M. Wu, S.-T. Chan, D. Mazumder, D. Tamborini, K. A. Stephens, B. Deng, P. Farzam, Y. Chu, M. A. Franceschini, J. Z. Qu, and S. A. Carp, "Improved accuracy of cerebral blood flow quantification in the presence of systemic physiology cross-talk using multi-layer Monte Carlo modeling," Neurophotonics **8**(1), 015001 (2021).
71. Y. Shang, Y. Zhao, R. Cheng, L. Dong, D. Irwin, and G. Yu, "Portable optical tissue flow oximeter based on diffuse correlation spectroscopy," Opt. Lett. **34**(22), 3556–3558 (2009).
72. D. Tamborini, P. Farzam, B. B. Zimmermann, K.-C. Wu, D. A. Boas, and M. A. Franceschini, "Development and characterization of a multidistance and multiwavelength diffuse correlation spectroscopy system," Neurophotonics **5**(1), 1–10 (2017).